

Article

Enhancing Mineral Exploration Programs Through Quantitative XRD: A Case Study from the Gumsberg Polymetallic Sulphide Deposits, Sweden

Sheida Makvandi ^{1,*} , Evelien Rost ¹, Thomas Witzke ¹, Matteo Pernechele ¹ and Hein Raat ²

¹ Application Competence Center, Malvern Panalytical B.V., 7602 EA Almelo, The Netherlands; evelien.rost@malvernpanalytical.com (E.R.); thomas.witzke@malvernpanalytical.com (T.W.); matteo.pernechele@malvernpanalytical.com (M.P.)

² EMX Royalty Corporation, 10001 W. Titan Road, Littleton, CO 80125, USA; hraat@emxroyalty.com

* Correspondence: sh.makvandi@gmail.com or sheida.makvandi@malvernpanalytical.com

Abstract: As challenges in precious and base metal exploration intensify due to the diminishing availability of high-grade ore deposits, rising demand, energy costs, and stricter regulations towards net-zero carbon activities, advanced techniques to enhance exploration efficiency are becoming increasingly critical. This study demonstrates the effectiveness of quantitative X-ray diffraction (QXRD) with Rietveld refinement, coupled with multivariate statistical analysis (including agglomerative hierarchical clustering, principal component analysis, and fuzzy analysis), in characterizing the complex mineralogy of strata-bound volcanic-associated limestone-skarn Zn-Pb-Ag-(Cu-Au)-type sulphide deposits (SVALS). Focusing on 113 coarse rejects from the Gumsberg project located in the Bergslagen mining district in central Sweden, the research identified five distinct mineralogical clusters corresponding to polymetallic base metal sulphide mineralization, its proximal alteration zones, and variably metamorphosed host rocks. The results reveal significant sulphide mineralization, ranging from disseminated to massive occurrences of sphalerite, pyrrhotite, pyrite, and galena, with trace amounts of secondary minerals like anglesite in certain samples indicating weathering processes. The study also identifies rare minerals such as armenite, often overlooked in traditional geological logging. These findings underscore the potential of QXRD to enhance resource estimation, optimize exploration strategies, and contribute to more efficient and sustainable mineral exploration programs. The accuracy of QXRD was cross-validated with geological logs and geochemical data, confirming its reliability as a mineralogical discrimination tool.

Keywords: quantitative XRD; Rietveld; cluster analysis; principal component analysis; HighScore Plus; polymetallic ore deposits; massive sulphides; precious metals; armenite; Gumsberg



Citation: Makvandi, S.; Rost, E.; Witzke, T.; Pernechele, M.; Raat, H. Enhancing Mineral Exploration Programs Through Quantitative XRD: A Case Study from the Gumsberg Polymetallic Sulphide Deposits, Sweden. *Minerals* **2024**, *14*, 1100. <https://doi.org/10.3390/min14111100>

Academic Editors: Teresa Pereira da Silva, Daniel P. S. De Oliveira and João Pedro Veiga

Received: 17 August 2024

Revised: 19 October 2024

Accepted: 21 October 2024

Published: 29 October 2024



Copyright: © 2024 by the authors. Licensee MDPI, Basel, Switzerland. This article is an open access article distributed under the terms and conditions of the Creative Commons Attribution (CC BY) license (<https://creativecommons.org/licenses/by/4.0/>).

1. Introduction

Accurate mineralogical characterization is the key to understanding the geological history and processes that led to the formation of mineral deposits, thereby guiding exploration strategies and optimizing resource extraction. This detailed analysis can reveal valuable information about the concentration of economically important minerals and the quality and quantity of ore. Furthermore, precise mineral quantification supports metallurgical processes by determining the best methods for mineral extraction and processing, ultimately enhancing the efficiency and profitability of mining operations.

Quantitative X-ray diffraction (QXRD) using the Rietveld method has emerged as a mineralogical characterization tool offering several advantages over traditional methods like optical microscopy and floor-standing SEM-EDS (Scanning Electron Microscopy–Energy Dispersive X-ray Spectroscopy) or MLA (Mineral Liberation Analyzer) [1–6]. Unlike optical microscopy, which depends heavily on the operator’s expertise and visual judgment, QXRD provides objective and reproducible identification and quantification of mineral

phases by analyzing diffraction patterns against extensive reference libraries. Compared to floor-standing SEM-EDS or MLA, QXRD allows the rapid processing of multiple samples. Additionally, the sample preparation for XRD is simpler, and the system operation requires minimal training [4–6]. Additionally, compact XRD systems are affordable and can be easily accommodated by most mining sites or exploration companies. It is important to note that, XRD, despite being a powerful mineralogical tool, has limitations when it comes to identifying specific mineral sub-members. While the closest matching structure is selected to explain certain peaks in the XRD pattern, the identified mineral names from supergroups (e.g., amphiboles, chlorite, biotite, zeolite) generally represent the broader group rather than specific sub-members. This limitation arises due to gaps in XRD databases, which often lack full structural coverage of the entire compositional range of these minerals. Additionally, factors like exsolution, twinning, cleavage, and parting can further complicate the interpretation of XRD data. In such cases, information from other techniques, such as XRF data to constrain the chemistry, become crucial for the cross-validation and confirmation of specific subgroup minerals.

Among various types of ore deposits, polymetallic sulphide deposits are paramount in supplying essential metals like zinc, lead, and copper [7], which are integral to modern society and play a significant role in various industrial applications, including construction, electronics, and transportation. With the demand for copper projected to double to 40 million tons in the next 20 years, the mining industry must invest heavily in discovering new mineral deposits to bridge this supply gap.

Despite their importance, the exploration of base metals presents numerous challenges. These deposits are often located in complex geological settings, necessitating advanced geophysical and geochemical techniques for accurate detection and delineation. The typically deep and remote locations of mineral deposits further escalate the costs and logistical difficulties of exploration. Additionally, managing environmental and regulatory concerns is crucial to ensure sustainable and responsible mining practices. Overcoming these obstacles requires adopting advanced, cost-effective, and time-efficient technologies to ensure the success of exploration programs and/or mining activities.

To exemplify the potential of QXRD and its practical application in exploration and mining programs, this study focuses on the mineralogical characterization of 113 coarse reject samples collected in the framework of the Gumsberg project (2016), located in the Bergslagen mining district in Central Sweden. The Gumsberg project is notable for its historic production, the apparent lack of modern exploration and drilling, and its high-grade styles of volcanogenic massive sulphide mineralization that have not been fully appreciated.

1.1. Geological Context

The Gumsberg property is located in the northern part of the Bergslagen district, a classical mining region mined for centuries. This district hosts thousands of mineral occurrences, prospects, and historic mine workings, with small to large iron oxide and polymetallic base metal sulphide mineralization being the most abundant and historically significant (Figure 1).

The Bergslagen district is an intensely mineralized part of a 280×300 km, Early Proterozoic felsic magmatic province characterized by polyphase deformation and medium- to high-grade metamorphism during the Svecokarelian orogeny (1.9–1.8 Ga). The region is interpreted as an intra-continental arc or back-arc extensional basin that developed above an active subduction zone [8–10]. The stratigraphy is marked by felsic meta-volcanic succession enveloped by siliciclastic metasedimentary rocks [10]. Marble interbeds in the upper meta-volcanic succession, which are former limestone, host many of the district's mineral deposits.

Various generations of syn-orogenic to post-orogenic intrusive rocks were emplaced between 1.91 and 1.75 Ga [9]. Significant hydrothermal alteration affected the supracrustal rocks [9,11] before extensive ductile deformation and regional metamorphism under upper

greenschist to amphibolite facies [12,13]. This led to significant changes in the deposits, including metal recrystallization and syn-tectonic remobilization [13–17].

The polymetallic sulphide deposits at Bergslagen are difficult to classify in terms of the major internationally recognized genetic classes of mineral deposits. Allen et al. [13] proposed that strata-bound volcanic-associated limestone-skarn Zn-Pb-Ag-(Cu-Au) sulphide deposits (SVALS) at Bergslagen were formed by the syn-volcanic subseafloor replacement of these shallow marine stromatolitic limestones, whereas the stratiform ash-siltstone (SAS) Zn-Pb-Ag polymetallic sulphide ores were formed by the deposition of metalliferous hydrothermal sediments between laminated, distal, deeper-water carbonate and felsic siltstone facies. Notable examples of SVALS-type deposits include the active Garpenberg Mine, Falun, Sala, and Stollberg deposits, which are commonly developed as systems of stratabound lenses, ranging in style from massive to vein networks and sulphide-cemented breccias with clasts of altered wall rock [18]. These deposits are typically rich in Zn, Pb, Ag, and sometimes Cu-Au. Sphalerite is the dominant mineral, with zones containing argentiferous galena, and in some areas, the mineralization shifts to chalcopyrite-rich zones with high pyrite and/or pyrrhotite contents [13].

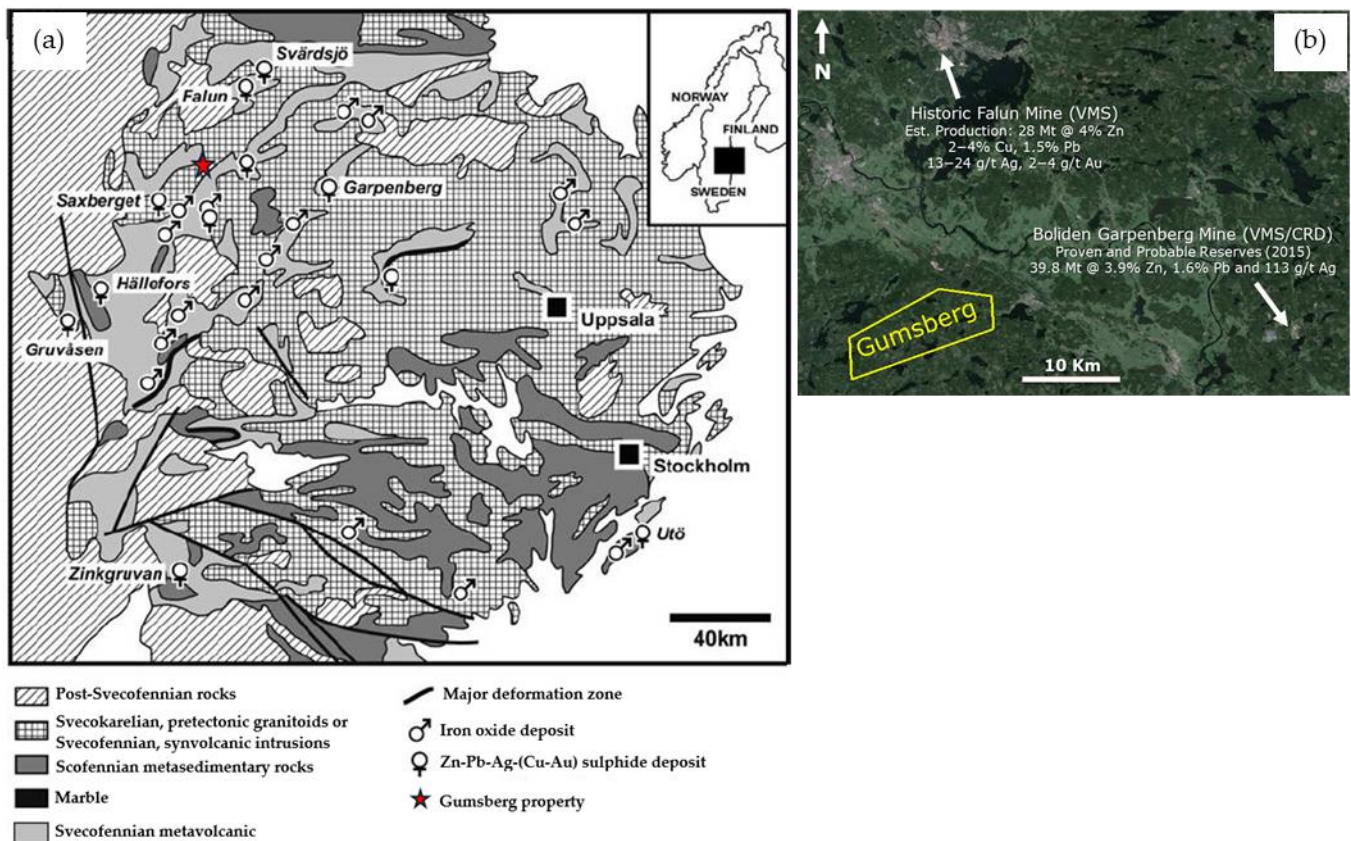


Figure 1. (a) Simplified bedrock geology of the Bergslagen ore province, showing principal mineral deposits (modified after Allen et al. [13]). (b) Location of the Gumsberg property in yellow in relation to the Falun Mine and Boliden’s Garpenberg Mine, within the Bergslagen mining district in central Sweden [19].

1.2. Local Geology

The Gumsberg project is located in the historic Bergslagen district, 30 km south of the world class Falun Mine (Zn-Pb-Cu-Au) and 30 km west of Boliden’s expanding Garpenberg Mine (Zn-Pb-Cu-Au-Ag; Figure 2). The property contains various polymetallic base metal sulphide prospects including over 30 historic mines that were actively mined from the 13th century until the early 1900s. This includes Östra Silverberg, Europe’s largest silver mine from 1300 to 1590. Massive sulphide mineralization within the Gumsberg property is

locally rich in silver and gold and dominated by sphalerite and galena. The prospects vary from steeply dipping remobilized massive sulphide veins, sub-seafloor replacement style hydrothermal mineralization, and exhalative mineralization to more disseminated feeder zone/stockwork style mineralization along a northeast trend [13,19]. Historical mining efforts suggest the mineralization is, partly structurally controlled, laterally continuous and forms pipe-like, moderate to steeply southeast plunging mineralized intervals [13].

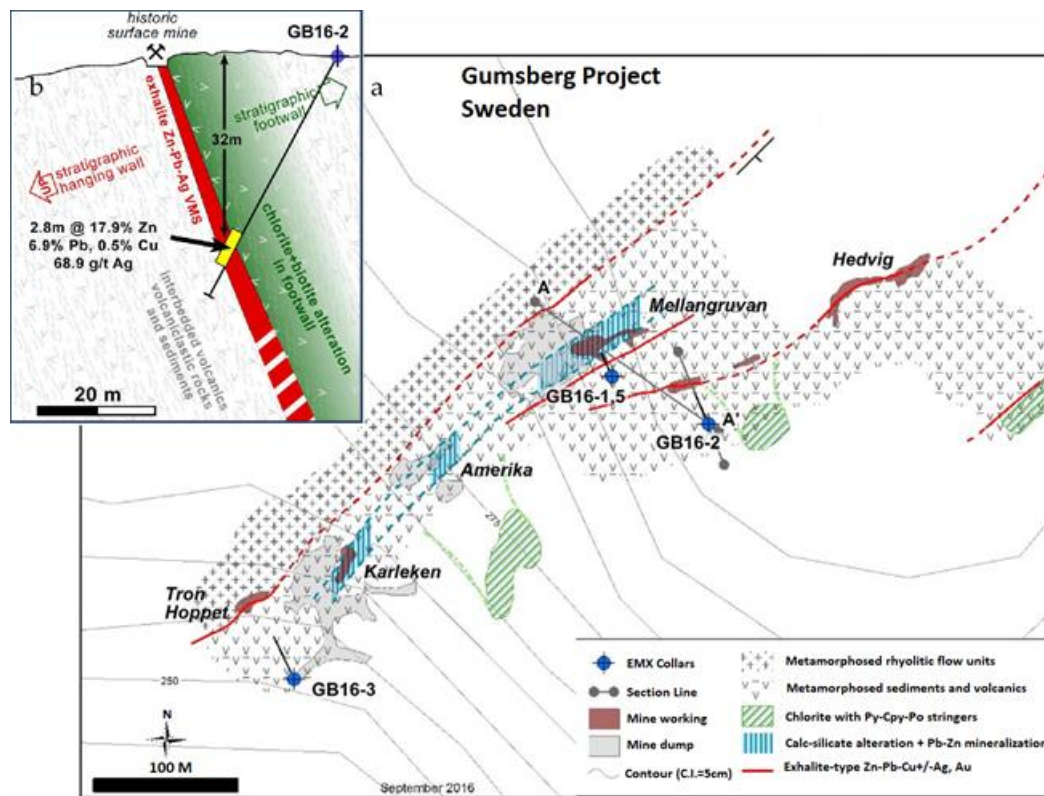


Figure 2. (a) Location of the four 2016 drill holes with high-grade intercepts (GB16-1, GB16-2, GB16-3, and GB16-5) within the Gumsberg property, part of the EMX Royalty Corp. exploration program in the Bergslagen mining district, southern-central Sweden. (b) Cross-section of drill hole GB16-2, looking towards the northeast [19].

Exploration drilling conducted by EMX Royalty Corp., a Canadian mineral prospect generator, in 2016, confirmed significant intervals of polymetallic Ag-Zn-Pb mineralization, with notable results from the Vallberget–Loberget trend (Figure 2). The Gumsberg property is now recognized for its 27 km of stratigraphy prospective for Ag-Zn-Pb mineralization, underscoring its potential for significant base and precious metal resources [19]. Figure 2 depicts the location of high-priority drill targets in the Vallberget–Loberget trend (GB16-1 to GB16-5 except GB16-4). The target drill hole GB-16-4 was a target in Gumsgruvan, another trend within the Gumsberg property, ~1–1.5 km NW of the Vallberget area.

2. Materials and Methods

2.1. Samples Description

This study analyzes 113 coarse reject samples from five reconnaissance diamond drill holes conducted by EMX Royalty Corp. in 2016. The high-priority drill targets were identified through comprehensive geological mapping and sampling. The drill holes were meticulously logged, and the selected samples provide a basis for this analysis, supported by detailed geological logs and chemical data, allowing for reliable cross-validation of QXRD results [19]. Figure 2 shows the location of drill holes GB16-1, GB16-2, GB16-3, and GB16-5 in the Vallberget–Loberget trend within the Gumsberg property. Figure S1a in the Supplementary Materials provides a plan view outcrop map indicating the locations of

the drill holes. The drill hole GB-16-4 is located in the Gumsgruvan area, ~1–1.5 km NW of Vallberget–Loberget. The sample descriptions, including the type of host rocks, ore mineralogy, and alteration mineral assemblages, are presented in Table 1. Sub-samples from all collected specimens were prepared and analyzed for trace element compositions in 2016 at ALS Global in Ireland. The analysis utilized Inductively Coupled Plasma Atomic Emission Spectroscopy (ICP-AES) with the ME-MS41 and ME-OG analytical packages, following an aqua regia digestion method. A summary of the analytical results is presented in Table 2. Table 2.

Table 1. Overview of geology and mineralogy of the 5 studied drill holes.

| Drill Hole ID | Depth (m) | Host Rock Type | Ore Mineralogy | Alteration Mineralogy |
|---------------|------------------------|-----------------------------------------------------------------------------------------------------------------|---------------------------------------------------------------------------------------------------------------------------------------------------|------------------------------------------------------------------------------------------|
| GB16-1 | 80–129 | Metasedimentary rocks (mostly metatuff and leptite) characterized by metavolcanic dykes | Replacement style Zn-Pb-Ag mineralization; Disseminated to massive sphalerite; Disseminated pyrite (traces) | Meta-breccia of clinozoisite and chlorite schist fragments; Quartz ± albite ± K-feldspar |
| including | 86.5–90.2 | Metavolcanics | Massive sphalerite and disseminated pyrite (<1%) | Amphibole and chlorite |
| GB16-1B | 120–129 | Fine grained tuffaceous laminated rocks underlain by massive, hard siliceous rock | Wispy zones of base metals. Disseminated pyrite; Galena and sphalerite in skarn rock, in breccia and carbonate veins with pyrrhotite on fractures | Quartz, K-feldspar, biotite, sericite, chlorite, and traces of garnet |
| GB16-2 | 31.3–31.8 36.9–39.7 | Meta-sedimentary rock (arkose) Massive sulphide (sphalerite) zone + 20% wall rocks | Hematite 5%–10% Massive sphalerite ± pyrite, galena | Actinolite, biotite, albite K-feldspar, chlorite, biotite, sericite, actinolite |
| GB16-3 | 52.5–61.7 | Relatively massive volcanic sandstone and siltstone metamorphosed to chlorite grade | Sulphide (1%–2%); Disseminations of pyrite (traces) | Quartz, albite, K-feldspar, chlorite, actinolite |
| including | 57.1–57.6 59.1–59.7 | Massive sulphide | Massive sulphide (fault banded) | K-feldspar, chlorite, actinolite |
| GB16-4 | 48–92.5 | Metavolcanics porphyritic, lithic tuffs | Disseminations of pyrite (1.00%–5.00%) ± pyrrhotite, magnetite | Quartz, amphibole, chlorite, sericite, cordierite ± epidote |
| GB16-5 | 26.1–29.1 | Tuffaceous fine-grained rock (Rhyolite?); Fine laminated siliceous rock grades into silica zone; Quartz breccia | Some pyrite within deformed bands of quartz-clinozoisite | Quartz, biotite, chlorite, clinozoisite |
| Including: | 27.1–28.1 | Massive sulphide | Massive sulphide (2/3 sphalerite, 1/3 galena, some chalcopyrite) to sulphide disseminations | Quartz, chlorite, iron oxides |
| Including: | 43.6–52.2 | Multiple stages of discordant breccias, some zones heterolithic with quartz vein fragments; Fine sediment/tuffs | Zn replacement zones, richer in clinozoisite rich lithologies | Clinozoisite ± chlorite ± quartz ± sericite |

A total of 29 coarse reject samples were selected from the drill holes GB16-1 and GB16-1B. The drill hole GB16-1 encounters metasedimentary rocks, metavolcanics, and fine-grained sediments. The presence of metavolcanic dykes and fractured textures indicates a complex geological history with multiple stages of deformation and mineralization (Tables 1 and 2). The dissemination of pyrite is observed, along with higher-grade intervals of pyrite, indicating potential zones of economic interest. The alteration minerals, such as clinozoisite, chlorite, and quartz, suggest a metamorphic overprint on the original mineralization, which is characteristic of the SVALS-type replacement-style sulphide mineralization in the region [13].

Table 2. High-grade mineralized zones in the sampled drill hole sections [19]. ^x: the true width is unknown. ^y: the true width is estimated to be 80%–90% of reported interval.

| Hole ID | Total Length (m) | Intercept Depth | | Intercept Length (m) | Pb (wt.%) | Zn (wt.%) | Ag (g/t) |
|-----------------------------------------------|------------------|---------------------------|------|----------------------|-----------|-----------|----------|
| | | From | To | | | | |
| GB16-1 ^x including GB16-1B | 152.5 | 84.5 | 92.7 | 8.2 | 0.1 | 4.6 | 2.3 |
| | | 86.5 | 90.2 | 3.7 | 0.1 | 8.9 | 4.4 |
| | | 120 | 129 | 9 | 0.2 | 0.6 | 3.6 |
| GB16-2 ^y | 46.2 | 36.9 | 39.7 | 2.8 | 6.9 | 17.9 | 68.8 |
| GB16-3 ^y including including | 58.8 | 52.5 | 61.7 | 9.2 | 0.5 | 3.7 | 7.3 |
| | | 57.1 | 57.6 | 0.5 | 4.1 | 28.5 | 51.4 |
| | | 59.1 | 59.7 | 0.6 | 2.3 | 16.4 | 39.3 |
| GB16-4 ^y | 110 | No Significant Intercepts | | | | | |
| GB16-5 ^y including including | 65 | 26.1 | 29.1 | 3 | 3 | 9.2 | 12.8 |
| | | 27.1 | 28.1 | 1 | 8.8 | 26.7 | 34.9 |
| | | 43.6 | 52.2 | 8.6 | 0.04 | 1.6 | 1.7 |

Fourteen samples were selected from the drill hole GB16-2 for this study. This hole intersects massive sulphide zones, particularly sphalerite-rich, which are fault-bounded. High grades of Zn (17.9%) and Pb (6.9%) with significant Ag (68.8 g/t) indicate substantial sulphide mineralization (Tables 1 and 2). The alteration assemblage of K-feldspar, chlorite, and biotite is consistent with intense hydrothermal activity typically associated with volcanogenic massive sulphide (VMS) deposits [19].

Fifteen samples from the study set were selected from the drill hole GB16-3. This drill hole shows relatively massive volcanic sandstone and siltstone, with brecciation indicating structural complexity (Table 1). Notable sulphide mineralization, with a high zinc content (up to 28.5% in specific intervals), suggests a robust sulphide system (Table 2). The presence of quartz, albite, and chlorite indicates hydrothermal alteration consistent with VMS mineralization processes.

From the drill hole GB16-4, 39 samples were studied for their mineralogical characteristics. The metavolcanic porphyritic and lithic tuffs characterized by disseminations of pyrite and occasional pyrrhotite and magnetite suggest dispersed sulphide mineralization in the host rocks (Table 1). Alteration minerals such as quartz and amphibole indicate moderate hydrothermal alteration.

Sixteen of the studied samples were from the drill hole GB16-5. The presence of tuffaceous fine-grained rock and quartz breccia points to a volcanic origin with significant fracturing. The high zinc (up to 26.7%) and lead (up to 8.8%) contents in the massive sulphide zones, along with significant silver (34.9 g/t), highlight the economic potential (Table 2).

The alteration minerals, including quartz and biotite, reflect intense hydrothermal activity. EMX Royalty Corp. [19] proposed that GB16-1 hosts replacement-style Zn-Pb-Ag mineralization, while GB16-2 and GB16-3 exhibit exhalative-style VMS mineralization. At GB16-5, the mineralization transitions from an exhalative style between 26.1 and 29.1 m to a replacement style between 43.6 and 52.2 m.

2.2. Analytical Methods

2.2.1. X-ray Powder Diffraction

X-ray powder diffraction is a versatile analytical method used for identifying and quantitatively determining the crystalline phases present in powdered and bulk samples. In this study, XRD scans of the 113 samples were collected at the Application Competence Centre, Malvern Panalytical, in the Netherlands, using the Minerals Edition of the Aeris compact X-ray diffractometer. This 600 W system was equipped with a cobalt-anode X-ray tube, a goniometer radius of 145 mm, 0.04 rad Soller slits, a 1/4° divergence slit, a 23 mm mask, a low beam-knife position, a step size of 0.02°, and an acquisition time of 79 s/step. The Bragg–Brentano measurement covered a range of 6–80° 2 θ , allowing the detection of

clay minerals and heavy minerals such as Fe oxides/hydroxides and sulphides. Cobalt radiation was used to prevent the emission of fluorescence, which occurs when using Cu radiation to analyze Fe, Cu, and/or Zn-containing materials. This choice improves the penetration depth of X-rays in the sample and enhances counting statistics. The use of a linear PIXcel^{1D} Medipix3 detector with an active length of $5.54^\circ 2\theta$ enables a scan acquisition time of just a few minutes.

2.2.2. XRD Data Analysis

Phase identification of all samples was performed using the all-in-one Malvern Panalytical's software suite, HighScore Plus, version 5.2 [20], with the ICDD PDF-5+ database [21]. The abundance of identified minerals in the analyzed samples was then determined using the Rietveld method [22]. Modern XRD quantification techniques, such as Rietveld analysis, provide a compelling alternative to classical peak intensity or area-based methods, as they do not require any standards or monitors. This method offers impressive accuracy and speed of analysis. The Rietveld method calculates structure factors based on atom positions in a crystal structure model, which can be adjusted during refinement [20,22]. However, the structure is often left unchanged and used to compute theoretical peaks and a profile. In this study, the Rietveld refinement included parameters such as scale factors, sample displacement, background coefficients, unit cell parameters, and Cagliotti W. For major minerals (over 10 wt.%) with preferential orientation, orientation parameters were also refined. To improve the fitting for abundant minerals, additional peak width functions (Cagliotti U and V) were refined when necessary. The final refinement model of an XRD scan, with proper parameter constraints, can serve as a template for analyzing similar samples, enabling automated and efficient quantitative XRD analysis of numerous samples. It is worth mentioning that understanding the exact crystal structure of all minerals present in the samples from the polymetallic base metal sulphide mineralization and associated alteration zones is essential for accurate Rietveld refinements.

2.2.3. Extended Cluster Analysis of XRD Data in HighScore Plus

Cluster analysis (CA) is designed to simplify the analysis of large datasets. By automatically sorting all closely related scans from an experiment into distinct groups, it identifies the most representative scan and the most outlying scans within each group [23,24]. Samples clustered together exhibit similar mineralogy, making it necessary to identify and quantify phases only in the most representative scan of each cluster. This allows for the creation of an efficient analytical routine, where other scans in the group can be automatically analyzed according to the established routine. This method is particularly effective for analyzing multiple samples from the same type of rocks or lithology and in quality control environments.

The CA tool in HighScore Plus exemplifies its comprehensive integration, allowing users to perform statistical analysis of XRD scans within the same software [1–4]. This eliminates the need for additional statistical software, streamlining workflows and enhancing efficiency in handling and interpreting large datasets. The module employs various algorithms, including correlation matrix creation, agglomerative hierarchical CA, grouping, and scan visualization. The process involves the following steps:

Comparison of Scans: All scans in a document are compared, resulting in a correlation matrix that represents the dissimilarities between data points of any given pair of scans.

Agglomerative Hierarchical Cluster Analysis: Scans are classified into different groups based on their similarity, producing a dendrogram where each scan starts as an individual cluster on the left side. Clusters merge stepwise until they form a single group.

Optimal Grouping Estimation: The best possible number of separate clusters is estimated using the KGS test or the largest relative step on the dissimilarity scale. This number can also be manually adjusted. The most representative scan and the two most outlying scans within each cluster are then identified and marked.

In addition to hierarchical clustering, three independent tools—Principal Components Analysis (PCA), Metric Multi-Dimensional Scaling (MMDS), and t-Stochastic Neighbor Embedding (t-SNE)—can be used to define clusters. These tools provide pseudo-three-dimensional plots for visualizing the clusters.

In this study, raw XRD patterns were analyzed using cluster analysis (CA) and principal component analysis (PCA) in HighScore Plus, without any correction or normalization, as all data were acquired on the same diffractometer. The CA algorithm classified the XRD patterns based solely on peak positions, ignoring peak intensities. Euclidean distances and the average linkage method were utilized for clustering [20]. The integration of CA and PCA could significantly enhance data analysis efficiency, and when combined with Rietveld refinement, this approach revealed hidden structural details and enabled comprehensive mineralogical characterization across multiple samples.

3. Results

3.1. XRD Pattern Analysis and PCA Results

The XRD patterns of 113 samples were analyzed using an extended approach in HighScore Plus. This method incorporated agglomerative hierarchical clustering, visualized in a dendrogram, along with three-dimensional principal component analysis (3D-PCA) and fuzzy analysis to classify and interpret the data. The 3D-PCA results are shown in Figure 3, with the corresponding scree plot displayed in Figure 3a. The scree plot illustrates the eigenvalues of the principal components, where a sharp decline after the first few components indicates that these capture the majority of the dataset's variance. This aids in determining the optimal number of components to retain (PC1 to PC3), as components beyond the “elbow” (PC4 to PC18) contribute minimally to the total variance (Figure 3a).

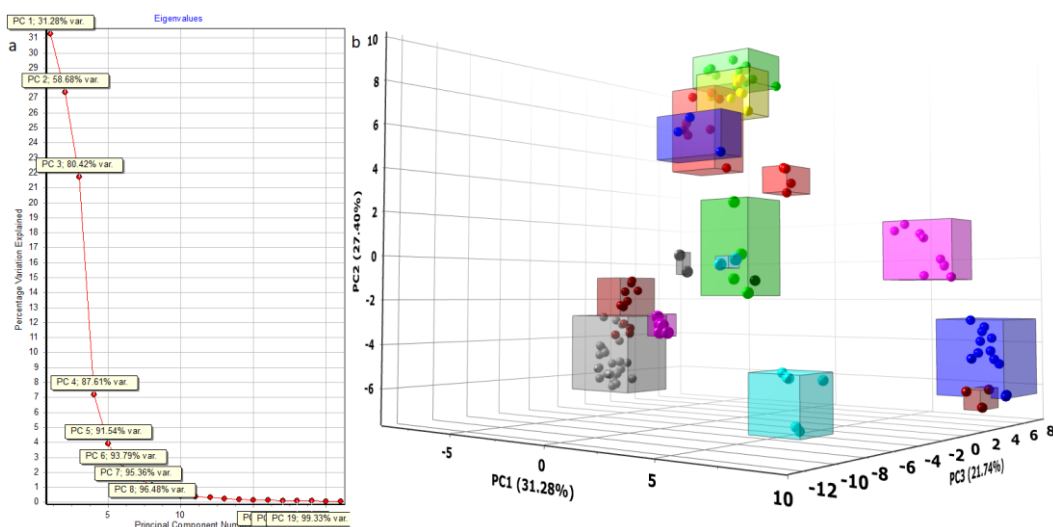


Figure 3. (a) Scree plot illustrating the eigenvalues of the principal components from the PCA, with the first three components accounting for 80.42% of the total variance (PC1: 31.28%, PC2: 27.40%, PC3: 21.74%). The x-axis denotes the principal components (PC1, PC2, . . . , PC21), while the y-axis represents the eigenvalues, indicating the percentage of variance explained. (b) 3D-PCA plot identifying fifteen clusters, and one non-clustered sample based on the analysis of 113 XRD scans. The x-axis displays the PCA scores, representing the transformed coordinates of the original data points in the reduced-dimensional space defined by the principal components. The colored clusters show data points as spheres, with each sphere representing a scan within that cluster.

As a result, the first three principal components collectively captured 80.4% of the total variance in the dataset, leading to the identification of 15 distinct mineralogical clusters, with 1 sample standing alone as a non-clustered outlier (Figure 3b). The most representative sample from each cluster was easily identified and it is marked with *** next to the scan name in the dendrogram (Figure S1b in the Supplementary Materials; this figure is not

included here due to the large number of samples, which would make the legend and sample names difficult to read). Figure 4 illustrates both an overlay and individual plots of the 15 representative scans alongside the non-clustered outlier. These 16 XRD patterns were imported into a new document in HighScore Plus to facilitate further analysis and the development of Rietveld models. These models were then used for automated data analysis of other samples within the same cluster.

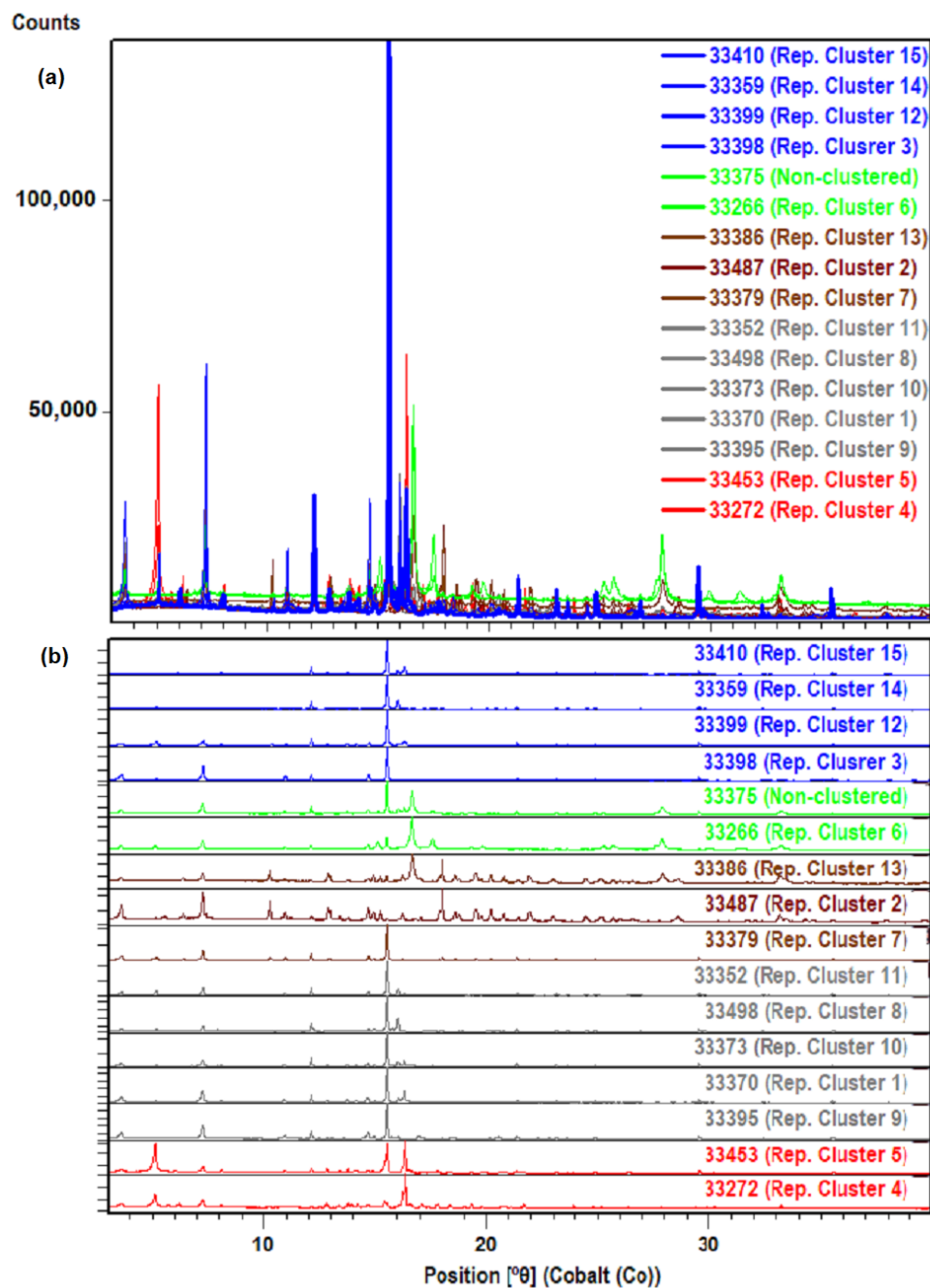


Figure 4. (a) An overlay view of the 15 representative and 1 outlier XRD patterns identified by the PCA in Figure 3b. (b) All 16 XRD patterns displayed separately, ordered and color-coded according to the 2nd cluster analysis (CA2) results.

3.2. Cluster Composition and Rietveld Refinement

As shown in Figures 3b and S2, certain clusters exhibit greater compositional similarity to one another, as indicated by the short distances between clusters in the latent variable space. This is also supported by fuzzy analysis (Table S1 in Supplementary Materials) re-

vealing that only five samples have probabilities (class membership) coefficients above 0.85 for Cluster 4, indicating they exclusively belong to this group, while four other samples are uniquely associated with Cluster 6. Additionally, the fuzzy analysis shows a probabilities coefficient above 0.85 for the non-clustered sample, confirming its status as an outlier. The remaining 103 samples exhibit membership coefficients between 0.15 and 0.85, suggesting that they could belong to more than one cluster.

Based on the extended CA results, it was possible to reduce the number of clusters by merging those with similar compositions. To further refine and optimize the selection of representative patterns for developing Rietveld models, a second cluster analysis (CA2) was conducted on the representative scans identified in the initial analysis (Figure 5). As a result, the 16 identified XRD patterns representing the 113 studied samples, including the outlier, were consolidated into five new groups. However, the dendrogram visualizing the agglomerative hierarchical clustering results reveals that samples within each group are connected by relatively longer tie bars compared to the first cluster analysis (CA1; Figure S2), indicating a greater degree of mineralogical variation within these groups.

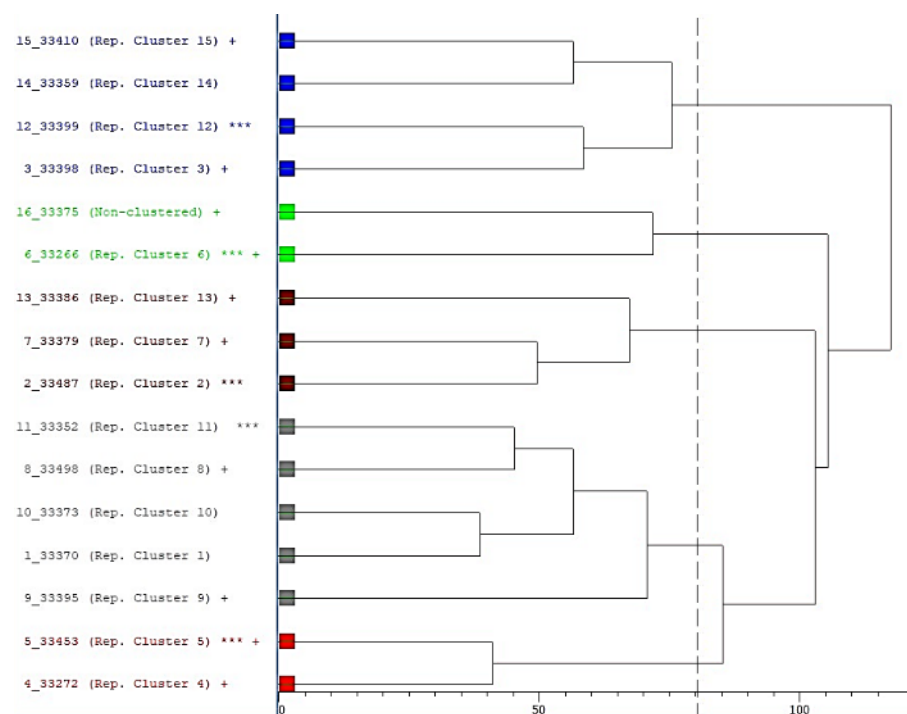


Figure 5. Visualization of agglomerative hierarchical clustering of XRD patterns representative of 15 clusters and the outlier resulted from CA1 in a tree-like fashion (dendrogram). In the dendrogram, the x-axis displays the dissimilarity of the tie bars, with each color representing a distinct cluster (Group 1: blue; Group 2: green; Group 3: brown; Group 4: gray; Group 5: red). The most representative scan and the two most outlying scans within each cluster are respectively marked by *** and +.

3.3. Fuzzy Clustering Prior to Rietveld Quantification

To explore the potential transitions between different mineralogical groups, fuzzy clustering was employed in HighScore Plus. Table 3 presents the membership matrix (M), detailing the calculated probabilities for each measurement. Notably, none of the analyzed samples exhibit a membership coefficient exceeding 0.85 for any of the five clusters, indicating that no sample exclusively belongs to a single cluster. However, all samples show coefficients above 0.48 for a particular cluster, suggesting a strong likelihood of association with that group [3,20]. Samples marked with an “x” in the mixture column likely contain mineral assemblages that are partially similar to those in other clusters. This mineralogical variation could be seen in the Rietveld quantification models (Figure 6). Moreover, indi-

vidual Rietveld models for the five identified groups are provided in the Supplementary Materials (Figures S1c–S5C). The full-pattern Rietveld quantification was performed on XRD scans of five samples, each representing one of the groups identified in CA2 (Figure 6). This method provided a comprehensive evaluation of the mineralogical composition within each group. By concentrating the Rietveld analysis on these representative samples, the mineralogical characterization of other samples within the corresponding group was both facilitated and automatically executed.

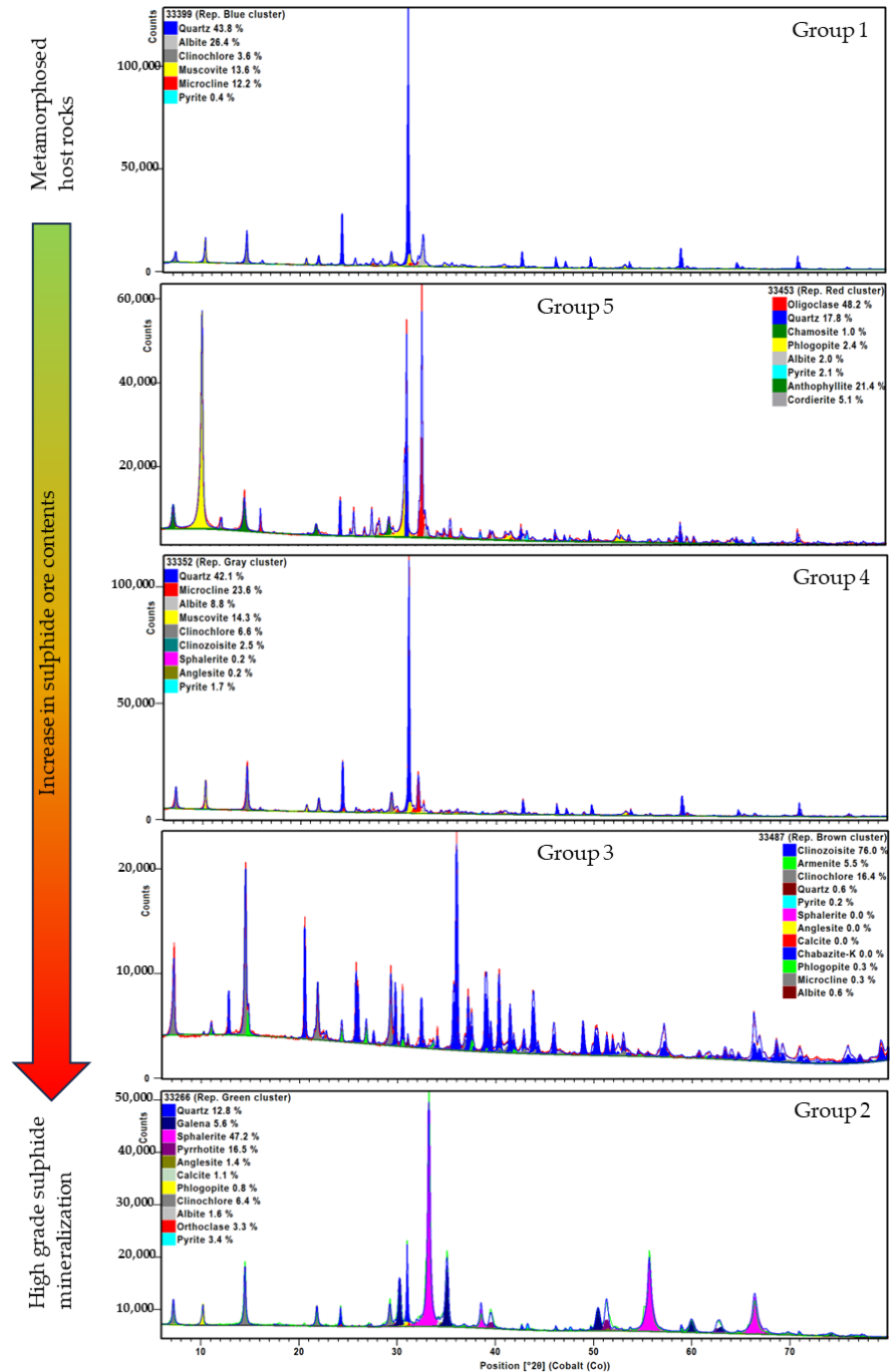


Figure 6. Full Rietveld pattern qualification of XRD scans for five samples, each representing one of the groups identified in CA2 (Groups 1 to 5 are highlighted in blue, green, brown, gray, and red, respectively). The graphs are arranged to illustrate the mineralogical changes from host rocks toward mineralization.

Table 3. Fuzzy clustering results for samples representing 15 clusters and 1 outlier following CA1. Probability coefficients are provided, with colors corresponding to the different clusters identified in Figures 4 and 5.

| Sample ID | Rep. CA1 | Cluster 1 | Cluster 2 | Cluster 3 | Cluster 4 | Cluster 5 | Mixture |
|-----------|---------------|-----------|-----------|-----------|-----------|-----------|---------|
| 33370 | Cluster 1 | 0.21 | 0.16 | 0.7 | 0.16 | 0.31 | x |
| 33487 | Cluster 2 | 0.06 | 0.09 | 0.2 | 0.87 | 0.16 | x |
| 33398 | Cluster 3 | 0.48 | 0.17 | 0.3 | 0.14 | 0.12 | x |
| 33272 | Cluster 4 | 0.13 | 0.16 | 0.29 | 0.21 | 0.68 | x |
| 33453 | Cluster 5 | 0.13 | 0.13 | 0.35 | 0.18 | 0.71 | x |
| 33266 | Cluster 6 | 0.07 | 0.58 | 0.16 | 0.2 | 0.16 | |
| 33379 | Cluster 7 | 0.13 | 0.01 | 0.44 | 0.69 | 0.2 | x |
| 33498 | Cluster 8 | 0.14 | 0.05 | 0.68 | 0.21 | 0.16 | |
| 33395 | Cluster 9 | 0.15 | 0.09 | 0.57 | 0.25 | 0.17 | x |
| 33373 | Cluster 10 | 0.27 | 0.38 | 0.69 | 0.12 | 0.2 | x |
| 33352 | Cluster 11 | 0.2 | 0.08 | 0.83 | 0.24 | 0.16 | |
| 33399 | Cluster 12 | 0.77 | 0.13 | 0.2 | 0.1 | 0.14 | |
| 33386 | Cluster 13 | 0.07 | 0.36 | 0.1 | 0.67 | 0.11 | |
| 33359 | Cluster 14 | 0.6 | 0.03 | 0.24 | 0.06 | 0.02 | |
| 33410 | Cluster 15 | 0.65 | 0.1 | 0.15 | 0.04 | 0.12 | |
| 33375 | Non-clustered | 0.26 | 0.83 | 0.33 | 0.15 | 0.1 | |

3.4. Variation in Mineralogical Characteristics Revealed by the QXRD Analysis

Phase identification and Rietveld quantification of the five XRD patterns identified as representative of all studied samples through a stepwise cluster analysis (CA1 and CA2) emphasize their distinct mineralogical compositions. As a result, Sample 33399, representing Group 1 in CA2 (Figure 5; also representative of Cluster 12 in CA1), is primarily composed of quartz, albite, microcline, clinocllore, and muscovite, with trace amounts of pyrite.

Unlike Group 1, for Group 2, the mineralogical analysis shows the highest degree of sulphide mineralization among the studied samples (Figure 6, Table 1). Rietveld quantification of Sample 33266, representative of this group (also representative of Group 6 in the initial cluster analysis), revealed a composition of 47.2% sphalerite, 16.5% pyrrhotite, 5.6% galena, and 3.4% pyrite, with a chemical composition inferred from stoichiometric formulas indicating 28.7% Zn and 5.8% Pb. Similarly, another member of Group 2, Sample 33375, exhibited high concentrations of Zn (20.8%) and Pb (2.8%).

Group 3 is defined by the variable dominance of clinozoisite, ranging from 36.0% to 76.0%, and the unique presence of minor amounts of armenite (2.1% to 5.5%). While sulphide ores are largely absent in the QXRD analysis reveals that Sample 33487, a representative of Group 3 in CA2 and Cluster 2 in CA1, lacks significant sulphide ores (also Cluster 2 in CA1), this sample is primarily composed of clinozoisite (76%), armenite (5.5%), and clinocllore (16.4%).

As illustrated in Figure 5, the three members of Group 3 (highlighted in brown) exhibit varying degrees of similarity and dissimilarity, as indicated by the differing lengths of the tie bars connecting them. Samples 33487 and 33379 (representing Cluster 7 in CA1) are linked by a short tie bar, indicating close compositional similarity, though Sample 33379 has lower clinozoisite (36.4%) and armenite (2.1%) contents and a notably higher proportion of quartz (39%) compared to the other two group members. In contrast, Sample 33386, the third member of Group 3, is connected by a longer tie bar in the dendrogram to its groupmates. Rietveld quantification showed that this sample has a distinct mineralogy with 15.1% sphalerite and dominant clinozoisite (72.4%).

Sample 33352, representative of Group 4, was retrieved from the drill hole GB16-1B as a coarse reject. The QXRD results revealed a mineral assemblage predominantly

consisting of quartz, microcline, albite, clinocllore, clinozoisite, muscovite, pyrite, and trace amounts of sphalerite (Figure 6). The QXRD results for Sample 33453, a Group 5 representative, also revealed a composition of 21.4% anthophyllite, 5.1% cordierite, 1% chamosite, 2.4% phlogopite, 17.8% quartz, 48.2% oligoclase, 2.0% albite, and 2.0% pyrite. The dendrogram in Figure 5 connects Group 5 to Group 1 by the longest tie bar, reflecting significant compositional dissimilarity between these groups (Figure 5).

4. Discussion

This study's results showed that stepwise hierarchical clustering and PCA of 113 XRD patterns greatly simplified data analysis by reducing the dataset into 16 representative patterns, grouped into five meaningful clusters (Figure 5 and Figure S2 in the Supplementary Materials). Fuzzy analysis served as a valuable complementary tool, not only further validating the distinct identities of certain clusters (e.g., Clusters 4 and 6 in CA1), but also revealing that the compositional boundaries between some clusters are not sharply defined, as indicated by the overlap in membership coefficients for most samples (Table 3 and Table S1 in the Supplementary Materials). The compositional overlap between different groups can be attributed to shared host rock types and/or geological events, such as hydrothermal activities or metamorphism, which play a role in the formation and/or alteration of mineral assemblages in this area [13–19]. As illustrated in Figure 5, Group 1 consists of four samples from coarse rejects of three different drill holes, hosted by metasedimentary, metavolcanic, and tuffaceous rocks (Tables 1 and 4). Despite their overall similarity, CA2 revealed internal variations: Samples 33410 (GB16-4) and 33359 (GB16-1B) are closely linked, and both are connected to Samples 33398 and 33399 (GB16-2) by a longer tie bar. This subgrouping reflects their geological origins, with the GB16-2 samples sharing metasedimentary host rocks, while the other two samples are primarily associated with metavolcanic rocks [19].

Table 4. Summary of ore mineral composition and chemistry as determined by Rietveld analysis of XRD patterns (QXRD), compared with the base metal content analyzed by ICP-AES. An asterisk (*) indicates the representative sample of each group. Accounting for the Pb content in the absence or scarcity of galena. Acronyms: G: group; Sph—sphalerite; Gn—galena; Py—pyrite; Armn—armenite; Phy—pyrrhotite. The colors in the 2nd CA clusters' column match those in Figure 5, while the columns presenting the ICP-AES, chemistry, and mineralogy by XRD–Rietveld results use a color scale, with red indicating the highest values and green the lowest.

| 2nd CA | DH | Depth (m) | Sample ID | ICP-AES (%) | | Chemistry_XRD-Rietveld (%) | | | | | Mineralog_XRD-Rietveld (%) | | | | |
|--------|---------|-------------|-------------------------|-------------|-----|----------------------------|-----|------|------|-----|----------------------------|-----|-----|------|------|
| | | | | Zn | Pb | Zn | Pb | Fe | S | Ba | Sph | Gn | Py | Armn | Pyh |
| G1 | GB16-1B | 139.0–140.0 | 33359 (Rep. Cluster 14) | 0.8 | 0.3 | 0.0 | 0.0 | 1.0 | 0.4 | 0.0 | 0.0 | 0.0 | 0.8 | 0.0 | 0.0 |
| | GB16-2 | 29.5–31.3 | 33398 (Rep. Cluster 3) | 0.1 | 0.0 | 0.0 | 0.0 | 2.1 | 0.2 | 0.0 | 0.0 | 0.0 | 0.4 | 0.0 | 0.0 |
| | GB16-2 | 31.3–31.8 | 33399 (Rep. Cluster 12) | 0.1 | 0.0 | 0.0 | 0.0 | 1.2 | 0.2 | 0.0 | 0.0 | 0.0 | 0.4 | 0.0 | 0.0 |
| | GB16-4 | 48.0–49.5 | 33410 (Rep. Cluster 15) | 0.0 | 0.0 | 0.0 | 0.0 | 0.2 | 0.0 | 0.0 | 0.0 | 0.0 | 0.4 | 0.0 | 0.0 |
| G2 | GB16-2 | 36.9–39.7 | 33266 (Rep. Cluster 6) | 9.2 | 0.3 | 28.7 | 5.8 | 15.8 | 24.6 | 0.0 | 47.2 | 5.6 | 3.4 | 0.0 | 16.5 |
| | GB16-3 | 59.1–59.7 | 33375 (Non-clustered) | 16.3 | 2.3 | 20.8 | 2.9 | 4.9 | 13.3 | 0.0 | 34.2 | 1.6 | 3.1 | 0.0 | 0.0 |
| G3 | GB16-1 | 79.5–80.5 | 33379 (Rep. Cluster 7) | 0.0 | 0.0 | 0.0 | 0.1 | 4.9 | 0.0 | 0.0 | 0.0 | * | 0.0 | 0.1 | 0.0 |
| | GB16-1 | 86.5–87.9 | 33386 (Rep. Cluster 13) | 10.7 | 0.1 | 10.1 | 0.0 | 4.2 | 5.0 | 0.6 | 15.1 | 0.0 | 0.0 | 4.7 | 0.0 |
| | GB16-5 | 46.7–47.2 | 33487 (Rep. Cluster 2) | 0.4 | 0.0 | 0.0 | 0.0 | 0.0 | 6.5 | 0.1 | 0.7 | 0.0 | 0.2 | 5.5 | 0.0 |
| G4 | GB16-1 | 128.0–129.0 | 33352 (Rep. Cluster 11) | 0.4 | 0.2 | 0.1 | 0.1 | 2.4 | 1.0 | 0.0 | 0.2 | * | 1.7 | 0.0 | 0.0 |
| | GB16-1 | 120.0–122.0 | 33498 (Rep. Cluster 8) | 0.1 | 0.4 | 0.0 | 0.0 | 2.0 | 1.0 | 0.0 | 0.0 | 0.0 | 1.9 | 0.0 | 0.0 |
| | GB16-2 | 27.4–28.0 | 33395 (Rep. Cluster 9) | 0.1 | 0.0 | 0.0 | 0.0 | 3.7 | 1.0 | 0.0 | 0.0 | 0.0 | 1.9 | 0.0 | 0.0 |
| | GB16-3 | 55.2–57.1 | 33370 (Rep. Cluster 1) | 0.2 | 0.0 | 0.0 | 0.5 | 2.3 | 0.9 | 0.0 | 0.0 | * | 1.5 | 0.0 | 0.0 |
| | GB16-3 | 58.1–59.1 | 33373 (Rep. Cluster 10) | 2.3 | 0.3 | 0.9 | 0.3 | 2.1 | 1.3 | 0.0 | 1.3 | * | 1.6 | 0.0 | 0.0 |
| G5 | GB16-4 | 66.0–67.0 | 33272 (Rep. Cluster 4) | 0.0 | 0.0 | 0.0 | 0.0 | 5.1 | 1.3 | 0.0 | 0.0 | 0.0 | 2.4 | 0.0 | 0.0 |
| | GB16-4 | 56.5–58.0 | 33453 (Rep. Cluster 5) | 0.0 | 0.0 | 0.0 | 0.0 | 3.4 | 1.1 | 0.0 | 0.0 | 0.0 | 2.0 | 0.0 | 0.0 |

Similarly, Group 4 consists of five samples from three different drill holes, predominantly hosted by metasedimentary rocks. CA2 analysis also revealed internal variations, with Samples 33352 and 33498 (both from GB16-1 but collected at different depths and hosted by poorly mineralized metasedimentary rocks containing mostly disseminated pyrite) forming a distinct subgroup. This subgroup is connected by a longer tie bar to Sam-

ples 33370 and 33373 (GB16-3), which originates from volcanic sandstone and siltstone with disseminated pyrite and sphalerite. Sample 33395 (GB16-2) links these two subgroups with another long tie bar. Additionally, the QXRD results in Table 4 strongly correlate with the CA findings, demonstrating that distinct mineralogical and compositional characteristics of the samples were key factors in their grouping. Additionally, variations within the groups reflect the individual mineralogy of each sample.

4.1. Mineralogical Signature of Host Rocks

The mineralogical composition of certain clusters demonstrates a strong correlation with their associated host rocks. For example, the mineralogy of Sample 33399, representative of Group 1, closely mirrors that of its fine-grained, tuffaceous laminated host rocks [19]. The presence of quartz, K- and Na-feldspars, chlorite, and muscovite (Figure 5) is consistent with host rocks that have undergone greenschist facies metamorphism. Additionally, the trace amounts of pyrite detected in this sample by QXRD align with the localized occurrence of base metal zones, where pyrite dissemination is a common feature in the host rocks [19]. This mineralogical alignment reinforces the relationship between cluster composition and geological processes. As shown in Table 4, the chemical composition of this sample, calculated from the stoichiometric formula of the identified minerals, strongly correlates with the ICP-AES results.

Although Group 5 exhibits significant compositional dissimilarity compared to Group 1, as illustrated by the longest tie bar in Figure 5, it is nonetheless characterized by a mineral assemblage (Figure 6) that reflects the typical mineralogy of Gumsberg metamorphosed host rocks (Table 1). Sample 33453, representative of this group, is a coarse reject from the drill hole GB16-4 at a depth of 48.0–92.0 m within metavolcanic porphyritic lithic tuffs (Table 1). These rocks have undergone intense hydrothermal alteration, which was later overprinted by strong polyphase deformation and metamorphism during the Svecokarelian orogeny [9,11–13].

Although the given sequence of events complicates the interpretation of the local geology and the understanding of paragenetic sequence of minerals [15], the significant presence of oligoclase and quartz in Sample 33453 (Figure 6) suggests that the original volcanic material was likely felsic in composition, consistent with the felsic metavolcanic rocks that characterize the region's lithotectonic unit [15–19]. The occurrence of anthophyllite and cordierite indicates that these rocks have undergone high-grade metamorphism, likely reaching amphibolite facies conditions [25]. Anthophyllite, a product of magnesium-rich environments, points to the mafic components within the original volcanic tuffs, while cordierite's presence suggests that the rocks were subjected to high temperatures, possibly due to proximity to syn-orogenic or post-orogenic intrusions. The minor amounts of phlogopite and chamosite further indicate a history of both prograde and retrograde metamorphism, with chamosite hinting at a retrograde phase as the region cooled and the higher-grade minerals began to break down [25]. Additionally, the presence of pyrite, although minor, suggests that the rocks were subjected to hydrothermal alteration, which aligns with the known history of significant hydrothermal activity in the Bergslagen district, which played a crucial role in metal recrystallization and remobilization during regional metamorphism [13,18,19].

4.2. Mineralogical Signature of Proximal Alteration Zones Revealed by the QXRD Data

Unlike Groups 1 and 5, which reflect the mineralogical signature of host rocks, Groups 3 and 4 represent a transition from metamorphic alteration zones to proximal sulphide mineralization (Figure 6). The QXRD results reveal a mineral assemblage predominantly consisting of quartz, microcline, and albite, alongside clinocllore, clinozoisite, muscovite, pyrite, and trace amounts of sphalerite (Figure 6). This mineralogy aligns with the host environment (Table 1), reflecting a history of intense hydrothermal alteration, sulphide deposition, followed by deformation and metamorphism during the Svecokarelian orogeny [15]. The abundance of silicate minerals suggests derivation from siliceous to tuffaceous rocks, while the presence of clinozoisite, clinocllore, and muscovite indicates a

metamorphic overprint [10–13]. The occurrence of pyrite and sphalerite suggests proximity to underlying massive sulphide zones. Figure 7 compares the XRD patterns of Group 3 samples with mineral variations corresponding to massive clinozoisite and replacement-style sphalerite mineralization [13–17]. As illustrated, armenite variably occurs in these samples.

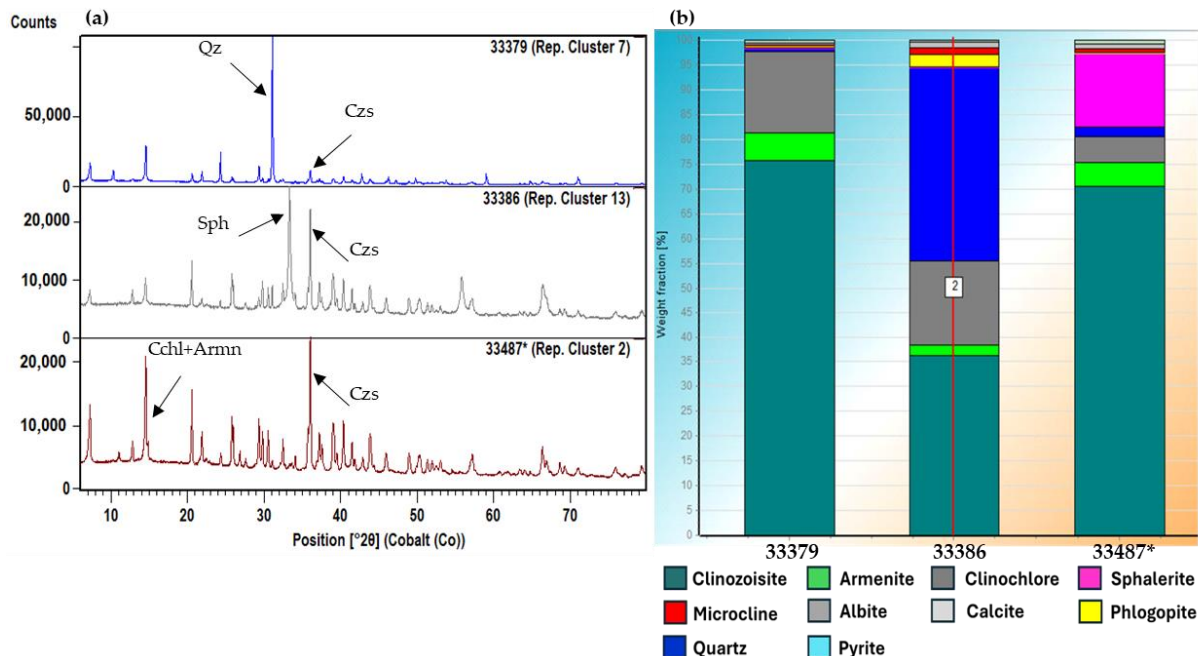


Figure 7. (a) 2D view of the distinct XRD patterns for samples clustered into Group 3 (highlighted in brown) in CA2. The most intense peak of each key mineral is marked. Acronyms—Qz: quartz; Czs: clinozoisite; Sph: sphalerite; Cchl: clinochlore; Armn: armenite. Armenite and clinozoisite have overlapping peaks. (b) Histograms illustrate the variable abundance of identified minerals in these samples. * Indicates the Group’s representative scan.

In contrast to QXRD, the geological log data do not report the presence of armenite in the Group 3 samples. The ICP-AES analysis also measured average Ba concentrations of 0.2% and 0.5%, respectively, in some samples from the drill holes GB16-1 (80.5 to 92.7 m depth) and GB16-5 (28.1 to 47.2 m depth). Additionally, elevated Ba concentrations, typically occurring as barite and/or Ba-bearing feldspars, have been observed in other studied areas from the Bergslagen district [26,27].

Armenite is a rare double-ring silicate hydrate from the milarite-osumilite group containing barium, aluminum, and calcium with the formula of $\text{BaCa}_2\text{Al}_6\text{Si}_9\text{O}_{30} \cdot 2\text{H}_2\text{O}$. It forms under low- to medium-grade metamorphic conditions, typically involving significant fluid–rock interaction, where barium-rich fluids interact with calcium-rich host rocks [28–31]. Skarn zones are common environments for its formation [28–31]. Dario et al. [28] reported the occurrence of armenite in the Rosas mine area (Mitza Sermentus mineworks, southwest Sardinia). They identified armenite-bearing samples collected along the contact zone between a sulphide-mineralized skarn vein and the black phyllite host rock. The black phyllite matrix primarily consists of muscovite, chamosite, and quartz, with feldspars, clinozoisite, titanite, and calcite as accessory phases. Gaspar and Inverno [30] also documented the occurrence of armenite alongside clinozoisite in the distal strata-bound scheelite skarns at the Riba de Alva Mine in Northeastern Portugal. They observed that armenite was present within the mineralized skarn zones, where it was sometimes intergrown with or replacing clinozoisite. Armenite also occurs in outcrops of leucocratic gneiss composed of celsian, margarite, quartz, white mica, and zoisite in the Berisal Complex, Swiss Central Alps. The estimated conditions for its formation were temperatures between 280 and 320 °C and pressures ranging from 2.0 to 2.6 kbar [30]. Dario et al. [29] emphasized three key reasons why armenite merits further

investigation beyond its apparent rarity and distinctive crystal structure: (1) Genesis Insight: Understanding armenite's formation could provide valuable information about the pressure–temperature–fluid conditions in the rocks where it occurs, which are often mineralized. (2) Potential Underestimation: Armenite is likely more common than previously believed, as it is difficult to identify using standard techniques and may frequently be overlooked in geological studies. (3) Indicator of Ba-rich Deposits: Given that armenite formation requires a primary barium source, its presence could indicate the proximity of Ba-rich mineral deposits.

4.3. QXRD Insights into the Mineralogical Signature of Massive Sulphides

In contrast to other groups, the mineralogy of Group 2 (in green), as determined by Rietveld quantification, indicates the highest grade of sulphide mineralization among the studied samples. This observation is consistent with both the geological log data [19] and the grade analysis results obtained by ICP-AES (Tables 1 and 2). The Rietveld analysis showed that Sample 33266, which represented Group 6 in the initial cluster analysis, predominantly consists of sphalerite, followed by pyrrhotite galena, and pyrite (Figure 6). The chemical composition inferred from the stoichiometric formulas of the identified minerals indicates this sample contains 28.7% Zn, and 5.8% Pb (Table 4). Similarly, another member of Group 2, Sample 33375, which was not clustered with any other samples in the CA1 due to its unique mineral composition, also shows high concentrations of Zn (20.8%) and Pb (2.8%). However, the ICP-AES analysis reported lower Zn contents for both samples in Group 2. Overall, XRD effectively captures the general trends in element concentrations, such as Zn, Pb, and Fe, as compared to ICP-AES. The discrepancy between the results from these two methods can be attributed to mineralogical heterogeneity within the mineralized zone, along with sample heterogeneity and the absence of homogenization procedures. These factors lead to variations in the compositions of the sub-samples analyzed by ICP-AES and XRD.

The stoichiometric calculation also reveals the presence of two Pb-bearing minerals in Sample 33266: galena and anglesite. Of the total 5.8% Pb measured in this sample by QXRD (Table 4), 4.8% is associated with the 5.6% abundance of galena, while approximately 1.0% is attributed to anglesite, which has an abundance of 1.4% in this sample (Figure 6). The occurrence of anglesite in sulphide mineralization zones raises questions about its origin. Anglesite (PbSO_4) typically occurs in two distinct forms, as identified by Zeng et al. [32]: (1) primary hydrothermal anglesite, which forms under low Pb/high S conditions, and (2) secondary supergene anglesite, which develops in high Pb/low S environments. Primary hydrothermal anglesite is found in the pores of precipitated hydrothermal fluids, often intergrown with pyrite and sphalerite. In contrast, secondary supergene anglesite forms through the low-temperature alteration of galena (PbS), frequently surrounding relict galena.

While further investigation using optical microscopy or SEM is needed to confirm the presence or absence of galena relics within anglesite, the occurrence of anglesite alone in some of the studied samples, particularly in association with sphalerite and pyrite (Group 2 and Group 3; Figure 6) likely suggests a primary hydrothermal origin. However, as shown in Figure 7, the presence of clinozoisite, albite, clinocllore, phlogopite, quartz, and trace amounts of calcite alongside anglesite and the sulphide ores reflects the region's complex geological history, characterized by hydrothermal mineralization, metamorphic overprinting, and subsequent weathering.

This finding serves as a reminder that while common minerals are consistently documented in geological log data, minor minerals like anglesite, which can have significant implications for mineral exploration, might not always be identified or noted. This oversight occurs because these minor minerals often appear in smaller quantities or are less visually distinctive, making them easier to overlook during routine logging processes. The experience of the logging geologist or petrographer plays a crucial role in being alert to the presence of certain minerals in specific geological settings.

Moreover, Table 4 indicates an elevated Fe content in Group 2 samples and other samples may correspond to various Fe-bearing phases, it is crucial to identify the specific minerals contributing to the overall Fe content (or other elements of interest). This level of insight allows for a more accurate interpretation of geochemical data, which is critical for precise economic resource estimation. The stoichiometric calculation (enabled by the chemistry calculator tool included in HighScore Plus [3,20]) provides detailed insights into the sample composition, enabling a thorough analysis of mineral phases and their elemental contributions. For instance, in Sample 33266, the stoichiometric calculation reveals that Fe is distributed across several mineral phases: 3% of Fe is present within the structure of sphalerite, approximately 10.2% in pyrrhotite, around 1.0% in clinocllore, and 1.6% in pyrite.

5. Conclusions

This study demonstrates the effectiveness of QXRD coupled with Rietveld refinement and extended cluster analysis in characterizing the complex mineralogy of the Gumsberg polymetallic sulphide deposit. The analysis identified five distinct mineralogical clusters, offering valuable insights into geological processes and alteration zones. Two clusters revealed mineralogical signatures of metamorphic host rocks, while two others indicated different proximal hydrothermal-metamorphic alteration zones—one with a variable base metal mineralization signature and another featuring massive clinzoisite and sub-sea floor replacement-style sphalerite mineralization. The fifth cluster also demonstrated the mineralogical characteristics of polymetallic sulphides. The detection of significant sulphide mineralization, particularly high levels of sphalerite, pyrrhotite, and galena, highlights the economic potential of the region. The presence of rare minerals like armenite, often missed in traditional methods, underscores the benefits of QXRD.

QXRD offers significant advantages as a complementary tool to traditional techniques such as optical microscopy, which rely on the petrography of a limited number of thin sections and the experience of the petrographer. QXRD allows for the rapid, high-throughput analysis of every sample, making it a time- and cost-efficient tool for exploration and mining. The straightforward sample preparation for QXRD further enhances its practicality. QXRD results can quickly (within minutes) identify samples needing further investigation, streamlining decision-making and improving the overall efficiency of exploration and mining programs. In this study, the accuracy of QXRD was cross-validated with geological logs and geochemical data obtained using the ICP-AES technique, confirming its reliability as a mineralogical discrimination tool.

Supplementary Materials: The following supporting information can be downloaded at: <https://www.mdpi.com/article/10.3390/min14111100/s1>, Figure S1: (a) Plan view outcrop map with location of drill holes including two cross-sections: (b) AA' through Vallberget-Loberget, and (b) BB' through Mellangruvan [17]. The historic holes, before 2016, are shown in gray. The red dots are the intersections for the 2016 drill holes. Note: the location of drill hole GB-16-4 is not seen in the images as it was a target in Gumsgruvan, another trend within the Gumsberg property, ~1–1.5 km NW of the Vallberget area. Figure S2: Dendrogram illustrating the agglomerative hierarchical clustering of 114 analyzed XRD patterns (1st cluster analysis). The XRD patterns are grouped into 15 clusters, with one outlier (sample 33375) remaining unclustered. Table S1: Results of fuzzy clustering of 113 XRD scans of studied samples. Probability/membership coefficients are provided. A coefficient ≥ 0.85 for any of the 15 clusters indicates that the sample exclusively belongs to that cluster; Figure S3c: Full Rietveld pattern quantification of XRD scan of sample 33399 representative of Group 1 in the 2nd cluster analysis (CA2); Figure S2c: Full Rietveld pattern quantification of XRD scan of sample 33453 representative of Group 5 in the 2nd cluster analysis (CA2). Figure S3c: Full Rietveld pattern quantification of XRD scan of sample 33352 representative of Group 4 in the 2nd cluster analysis (CA2); Figure S4c: Full Rietveld pattern quantification of XRD scan of sample 33379 representative of Group 3 in the 2nd cluster analysis (CA2); Figure S5c: Full Rietveld pattern quantification of XRD scan of sample 33266 representative of Group 2 in the 2nd cluster analysis (CA2).

Author Contributions: Conceptualization—S.M. and E.R.; Formal analysis—S.M., E.R. and T.W.; Investigation—S.M. and E.R.; Methodology—S.M., E.R., T.W. and M.P.; Validation—S.M.; Visualization—S.M.; Resources—H.R.; Writing—original draft preparation, S.M.; Writing—review and editing, S.M., E.R., T.W., M.P. and H.R. All authors have read and agreed to the published version of the manuscript.

Funding: This research received no external funding.

Data Availability Statement: Data are contained within the article.

Acknowledgments: We would like to extend our gratitude to EMX Scandinavia AB/EMX Royalty Corp. for their collaboration and for providing samples along with geological and geochemical databases. T. Degen and M. Sommariva are also thanked for their technical advice and support.

Conflicts of Interest: Sheida Makvandi, Evelien Rost, Thomas Witzke, and Matteo Pernechele are employees of the Application Competence Center. Also, Hein is an employee of Raat EMX Royalty Corporation. The paper reflects the views of the scientists and not the company.

References

1. Pernechele, M.; López, Á.; Davoise, D.; Maestre, M.; König, U.; Norberg, N. Value of Rapid Mineralogical Monitoring of Copper Ores. *Minerals* **2021**, *11*, 1142. [[CrossRef](#)]
2. König, U.; Degen, T.; Norberg, N. PLSR as a New XRD Method for Downstream Processing of Ores: Case Study: Fe₂ + Determination in Iron Ore Sinter. In *Powder Diffraction*; Cambridge University Press: Cambridge, UK, 2014; Volume 29, pp. S78–S83.
3. König, U. Nickel Laterites—Mineralogical Monitoring for Grade Definition and Process Optimization. *Minerals* **2021**, *11*, 1178. [[CrossRef](#)]
4. Makvandi, S.; Cauzid, J.; Tarantola, A.; Melfos, V.; Voudouris, P. XRD Clustering and Quantitative Analysis as a Fingerprinting Technique to Study Ore Deposits. In Proceedings of the 17th SGA Biennial Meeting 2023, Zürich, Switzerland, 28 August–1 September 2023.
5. Makvandi, S.; Pagé, P.; Tremblay, J.; Girard, R. Exploration for Platinum-Group Minerals in till: A New Approach to the Recovery, Counting, Mineral Identification and Chemical Characterization. *Minerals* **2021**, *11*, 264. [[CrossRef](#)]
6. Makvandi, S.; Beaudoin, G.; McClenghan, M.B.; Quirt, D.; Ledru, P. PCA of Fe-oxides MLA data as an advanced tool in provenance discrimination and indicator mineral exploration: Case study from bedrock and till from the Kiggavik U deposits area (Nunavut, Canada). *J. Geochem. Explor.* **2019**, *197*, 199–211. [[CrossRef](#)]
7. Franklin, J.M.; Gibson, H.L.; Jonasson, I.R.; Galley, A.G. Volcanogenic Massive Sulphide Deposits. In Proceedings of the 12th Biennial SGA Meeting, Uppsala, Sweden, 12–15 August 2013; pp. 523–560.
8. Barbosa, L.; Tiu, G.; Jansson, N.; Wanhainen, C.; Lilja, L.; Ghorbani, Y. Gold occurrence in the footwall of the Lappberget Deposit, Garpenberg Mine, Sweden. *Ore. Geol. Rev.* **2024**, *171*, 106174. [[CrossRef](#)]
9. Stephens, M.B. *Synthesis of the Bedrock Geology in the Bergslagen Region, Fennoscandian Shield, South-Central Sweden*; Sveriges Geologiska Undersökning (SGU): Uppsala, Sweden, 2009.
10. Stephens, M.B.; Jansson, N.F. Paleoproterozoic (1.9–1.8 Ga) syn-orogenic magmatism, sedimentation and mineralization in the Bergslagen lithotectonic unit, Svecokarelian Orogen. *Geol. Soc. Lond. Mem.* **2020**, *50*, 155–206. [[CrossRef](#)]
11. Allen, R.L.; Jansson, N.; Ripa, M. Bergslagen: Geology of the Volcanic-and Limestone-Hosted Base Metal and Iron Oxide Deposits. Excursion Guidebook Swe 4. In Proceedings of the 12th Biennial SGA Meeting, Uppsala, Sweden, 12–15 August 2013.
12. Vivallo, W. The geology and genesis of the Proterozoic massive sulfide deposit at Garpenberg, central Sweden. *Econ. Geol.* **1985**, *80*, 17–32. [[CrossRef](#)]
13. Allen, R.L.; Lundstrom, I.; Ripa, M.; Christofferson, H. Facies analysis of a 1.9 Ga, continental margin, back-arc, felsic caldera province with diverse Zn-Pb-Ag-(Cu-Au) sulfide and Fe oxide deposits, Bergslagen region, Sweden. *Econ. Geol.* **1996**, *91*, 979–1008. [[CrossRef](#)]
14. Jansson, N. The Origin of Iron Ores in Bergslagen, Sweden, and Their Relationships with Polymetallic Sulphide Ores. Ph.D. Thesis, Luleå Tekniska Universitet, Luleå, Sweden, 2011.
15. Jansson, N.F.; Allen, R.L. Multistage ore formation at the Ryllshyttan marble and skarn-hosted Zn-Pb-Ag-(Cu)+magnetite deposit, Bergslagen, Sweden. *Ore Geol. Rev.* **2015**, *69*, 217–242. [[CrossRef](#)]
16. Andersson, S.S.; Jonsson, E.; Hogdahl, K. Metamorphism and deformation of a Palaeoproterozoic polymetallic sulphide–oxide mineralisation: Hornkullen, Bergslagen, Sweden. *GFF* **2016**, *138*, 410–423. [[CrossRef](#)]
17. Kampmann, T.C.; Stephens, M.B.; Ripa, M.; Hellstrom, F.A.; Majka, J. Time constraints on magmatism, mineralisation and metamorphism at the Falun base metal sulphide deposit, Sweden, using U-Pb geochronology on zircon and monazite. *Precambrian Res.* **2016**, *278*, 52–68. [[CrossRef](#)]
18. Fahlvik, A.; Kampmann, T.C.; Jansson, N.F. Hydrothermal alteration, lithochemical marker units and vectors towards mineralisation at the Svärdsjö Zn-Pb-Cu deposit, Bergslagen, Sweden. *GFF* **2022**, *144*, 177–195. [[CrossRef](#)]

19. EMX Royalty Corp. *Gumsberg-Au-Cu (Zn-Pb) VMS Projects, Bergslagen District, Southern Sweden. Technical Marketing Report*; EMX Royalty Corp.: Vancouver, BC, Canada, 2016.
20. Degen, T.; Sadki, M.; Bron, E.; König, U.; Nénert, G. The High Score Suite. In *Powder Diffraction*; Cambridge University Press: Cambridge, UK, 2014; Volume 29, pp. S13–S18.
21. Gates-Rector, S.; Blanton, T. The Powder Diffraction File: A Quality Materials Characterization Database. *Powder Diffr.* **2019**, *34*, 352–360. [[CrossRef](#)]
22. Rietveld, H.M. A Profile Refinement Method for Nuclear and Magnetic Structures. *J. Appl. Crystallogr.* **1969**, *2*, 65–71. [[CrossRef](#)]
23. Kelley, L.A.; Gardner, S.P.; Sutcliffe, M.J. An automated approach for clustering an ensemble of NMR-derived protein structures into conformationally related subfamilies. *Protein Eng. Des. Sel.* **1996**, *9*, 1063–1065. [[CrossRef](#)]
24. Liao, B.; Chen, J. The application of cluster analysis in X-ray diffraction phase analysis. *J. Appl. Crystallogr.* **1992**, *25*, 336–339. [[CrossRef](#)]
25. Morrison, S.M.; Prabhu, A.; Hazen, R.M. An evolutionary system of mineralogy, Part VIII: The evolution of metamorphic minerals. *Am. Mineral.* **2024**, *109*, 1760–1784. [[CrossRef](#)]
26. Jansson, N.F.; Allen, R.L.; Skogsmo, G.; Turner, T. Origin of Palaeoproterozoic, sub-seafloor Zn-Pb-Ag skarn deposits, Sala area, Bergslagen, Sweden. *Miner. Depos.* **2021**, *57*, 455–480. [[CrossRef](#)]
27. Camitz, J.; Rauséus, G.; Jönberger, J.; Persson, L.; Sopher, D.; Bastani, M. *Characterisation of Mining Waste in Central and Southern Bergslagen, Sweden*; Geological Survey of Sweden: Uppsala, Sweden, 2024.
28. Dario, F.; Luca, D.M.; Antonio, A.; Fabrizio, C.; Antonio, F.; Stefano, N. Armenite: A Really Rare Mineral? In Proceedings of the 3rd European Mineralogical Conference EMC 2020, Cracow, Poland, 6–10 September 2020.
29. Gaspar, L.M.; Inverno, C.M.C. Mineralogy and metasomatic evolution of distal strata-bound scheelite skarns in the Riba de Alva Mine, Northeastern Portugal. *Econ. Geol.* **2000**, *95*, 1259–1275. [[CrossRef](#)]
30. Hetherington, C.J.; Mullis, J.; Graeser, S.; Gieré, R. Formation of Armenite in the Berisal Complex, Simplon Region, Switzerland. *Schweiz. Mineral. Petrogr. Mitteilungen* **2003**, *83*, 243–259.
31. Ray, G.L.E.; Webster, I.C.L. *Skarns in British Columbia. Geological Survey of British Columbia*; Geological Survey Branch: Reston, VA, USA, 1997.
32. Zeng, Z.; Chen, Z.; Qi, H. Two Processes of Anglesite Formation and a Model of Secondary Supergene Enrichment of Bi and Ag in Seafloor Hydrothermal Sulfide Deposits. *J. Mar. Sci. Eng.* **2022**, *10*, 35. [[CrossRef](#)]

Disclaimer/Publisher’s Note: The statements, opinions and data contained in all publications are solely those of the individual author(s) and contributor(s) and not of MDPI and/or the editor(s). MDPI and/or the editor(s) disclaim responsibility for any injury to people or property resulting from any ideas, methods, instructions or products referred to in the content.